

# Tailoring Chain-Length in Through-Space Charge-Transfer Donor- $\sigma$ -Acceptor Multifunctional Emitters for Efficient Long-Term Bioimaging

Tapashi Sarmah, Soumik Pal, Debasish Barman, Debika Barman, Bithiah Grace Jaganathan,\* and Parameswar Krishnan Iyer\*

This work presents a simple strategy to develop a new series of through-space charge-transfer (TSCT) donor–acceptor luminogens with varying alkyl chain lengths as spacer groups (D- $\sigma$ -A), CzNDPy [5-(4-(9H-carbazol-9-yl)alkyl)-5H-pyrazino[2,3-b] indole-2,3-dicarbonitrile] ( $n = 2, 3, 4,$  and  $5$ ) displaying rare multifunctional optical behaviors of aggregation-induced emission (AIE), thermally activated delayed fluorescence (TADF), aggregation-induced delayed fluorescence (AIDF), mechanoluminescence (ML), and mechanochromism (MCL) properties. Fine-tuning the flexible chain lengths between donor and acceptor results in variable intermolecular interactions and charge transfer (CT) behavior, thereby modulating their respective optical properties in aggregated/solid states. The integrated emitters exhibit a maximum total quantum yield of 85% with a prolonged lifetime of 344  $\mu$ s. Considering the challenges existing for developing AIDF molecules with longer lifetimes, enhanced fluorescence efficiency, and tunable emission characteristics, their utility is emphasized for efficient long-term bioimaging of human breast cancer cells up to 7 days. These molecules constitute the first examples of multifunctional organic TSCT AIDF small molecules with such long lifetimes, tunable emission colors, and higher fluorescence efficiency used for the diagnostic imaging of cancer cells. This study also sheds light on the structure-property relationships and offers valuable insights into the new class of tailored optical materials for various applications.

anti-counterfeiting, and cancer therapeutics.<sup>[1]</sup> Developing multifunctional organic TADF materials with longer lifetime and higher photoluminescence quantum efficiency (PLQY) are still in infancy phase because of the involvement of many non-radiative pathways in multiple process.<sup>[2]</sup> Among the different strategies for developing efficient TADF, constructing donor-acceptor moieties directly (commonly known as through-bond charge transfer, TBCT) or incorporating electronically benign conjugated spacer groups (D- $\pi$ -A) and non-conjugated groups (D- $\sigma$ -A) for through-space charge transfer (TSCT) is more popular and convenient.<sup>[3]</sup> TBCT-based multifunctional TADF emitters often have disadvantages in balancing lifetime and PLQY due to their larger  $\Delta E_{ST}$  values.<sup>[4]</sup> In TSCT systems, the spacer group not only minimizes the overlap between the highest occupied molecular orbital (HOMO) and lowest unoccupied molecular orbital (LUMO) leading to a very small singlet-triplet energy gap ( $\Delta E_{ST}$ ) but also enhances the radiative decay rate, ensuring a high PLQY.<sup>[5]</sup> Although many D- $\pi$ -A type multifunctional

TSCT-based TADF-active emitters have been investigated, particularly for use in solution-processable OLEDs, D- $\sigma$ -A systems with flexible spacer groups are rare, especially among small TADF molecules.<sup>[6]</sup> In terms of molecular design of such systems, donors like carbazole and acridan and acceptors such as sulfone, triazine, carbonyl, or boron-fused heterocycles, are the most explored.<sup>[3]</sup> Some examples of carbazole-based D- $\sigma$ -A TADF AIEgens include XCT, XtBuCT, 2, and 1, reported by

## 1. Introduction

Multifunctional pure organic thermally activated delayed fluorescence luminogens with AIE, AIDF, room temperature phosphorescence (RTP), ML, and MCL properties have gained significant importance in recent years owing to their low cost, environmental friendliness, and widespread applications in the fields of bioimaging, organic light-emitting diodes (OLEDs), sensors,

T. Sarmah, D. Barman, D. Barman, P. K. Iyer  
Department of Chemistry  
Indian Institute of Technology Guwahati  
Guwahati, Assam 781039, India  
E-mail: [pki@iitg.ac.in](mailto:pki@iitg.ac.in)

 The ORCID identification number(s) for the author(s) of this article can be found under <https://doi.org/10.1002/adom.202403060>

DOI: 10.1002/adom.202403060

S. Pal, B. G. Jaganathan  
Department of Biosciences and Bioengineering  
Indian Institute of Technology Guwahati  
Guwahati, Assam 781039, India  
E-mail: [bithiahgj@iitg.ac.in](mailto:bithiahgj@iitg.ac.in)

P. K. Iyer  
Centre for Nanotechnology  
Indian Institute of Technology Guwahati  
Guwahati, Assam 781039, India

different research groups, with compound 1 showing the highest PLQY of 92%, a delayed lifetime of 6.8  $\mu\text{s}$ , and a  $k_{\text{RISC}}$  (rate constant of reverse intersystem crossing process) value of  $9.9 \times 10^5 \text{ s}^{-1}$ .<sup>[7]</sup> Recently, a series of multifunctional TSCT emitters with tunable alkyl chains, BT2OxCz, were reported, exhibiting a highest PLQY of 13.3% and a longest delayed lifetime of 55  $\mu\text{s}$ .<sup>[8]</sup> These findings highlight the need to develop new acceptor cores, presenting a vital challenge to achieve both higher PLQY and longer lifetimes within a single multifunctional emitter, an area that has attracted significant research interest in recent years.

In addition, TADF active AIEgens rarely display some unusual stimuli-responsive behaviors like ML (an interesting emission process activated by mechanical stimulation) and MCL (reversible emission color change upon external stimuli), which primarily occur due to the subtle modifications in molecular packing caused by external stimuli.<sup>[9]</sup>

Conventional fluorescence imaging is demonstrated as a versatile and essential tool for clinical diagnostics and biomedical research. It provides high resolution and sensitive images as compared to other imaging techniques which allows dynamic and detailed quantitative information at the subcellular level.<sup>[10]</sup> Metal-free organic probes which possess broader absorption spectra and large Stokes shift (usually over 80 nm) provide more cost-effective, environmentally friendly, and safer alternative to traditional metal complex-based imaging agents which often face issues like complex synthesis, high cost, and toxicity. Currently, integrating the TADF features with AIE characteristics in a single molecule termed as AIDF is regarded as a promising probe in bioimaging because of their low cytotoxicity, high PLQY, enhanced brightness, tunable emission wavelengths, and stability.<sup>[11]</sup> With longer lifetimes and higher quantum efficiencies, these molecules enable selective signal detection while minimizing interference from autofluorescence in biological tissues.<sup>[12]</sup> Although many AIDF molecules have been reported for bioimaging, TSCT-based AIDF small molecules have yet to be explored. Herein we provide an effective strategy to acquire a set of highly efficient small molecule TSCT AIDF emitters with longer lifetimes and tunable photophysical properties and shed light by using them for long-term bioimaging. In this context, we have explored an improved and simple design strategy for achieving a new class of D- $\sigma$ -A type multifunctional TADF materials denoted as CznDPy ( $n = 2, 3, 4$ , and 5). By designing a novel acceptor and incorporating alkyl chains of varying lengths as spacer groups between donor and acceptor to modulate the steric hindrance and CT, we achieved multiple optical properties TSCT, TADF, AIE, AIDF, ML, and MCL in a single molecule. They exhibit the smallest  $\Delta E_{\text{ST}}$  value of 0.0003 eV, a long lifetime of up to 344  $\mu\text{s}$ , and the highest total PLQY of 85%. Interestingly, we observed even-odd effects of alkyl chains, an unusual phenomenon in their TSCT, AIE, AIDF, and TADF behaviors. With their outstanding AIDF nature and cell viability, we have successfully utilized them for efficient long-term imaging of human breast cancer cells MDA-MB-231 up to 7 days. To the best of our knowledge, these molecules are the first examples of even-odd alkyl chain modulated D- $\sigma$ -A type multifunctional TSCT TADF small molecules with such low  $\Delta E_{\text{ST}}$  values, higher quantum yields, and longer lifetimes. For the first time, we have shown the structure-property relationships and used these TSCT type AIDF molecules for efficient long-term bioimaging. Through this work,

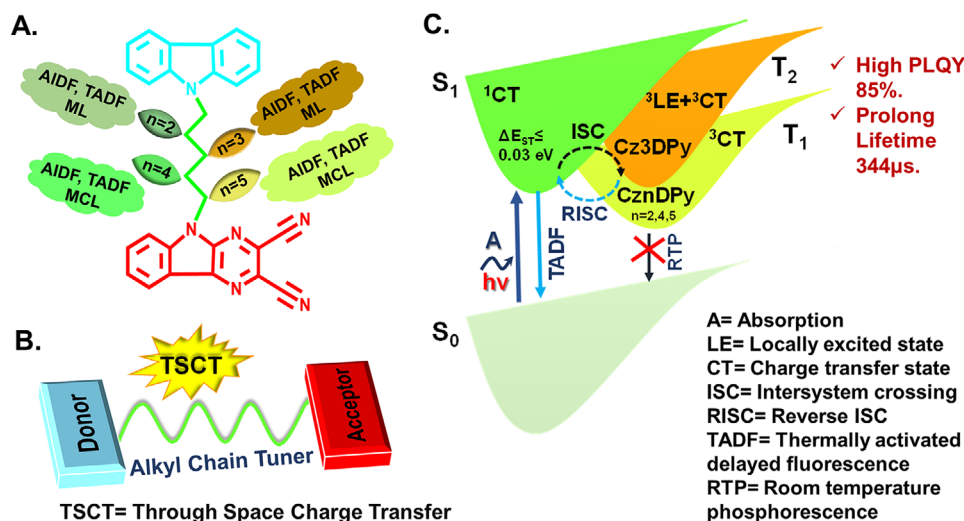
a new class of TADF materials is introduced focusing systematically on TSCT excited states, and a mechanistic approach is derived to demonstrate the relationship between their structures and properties for diagnostic live imaging of cancer cells.

## 2. Results and Discussion

A series of donor-alkyl spacer-acceptors (D- $\sigma$ -A), CznDPy ( $n = 2, 3, 4$ , and 5) namely, 5-(3-(9H-carbazol-9-yl) ethyl)-5H-pyrazino[2,3-b] indole-2,3-dicarbonitrile (Cz2DPy), 5-(3-(9H-carbazol-9-yl) propyl)-5H-pyrazino[2,3-b] indole-2,3-dicarbonitrile (Cz3DPy), 5-(3-(9H-carbazol-9-yl) butyl)-5H-pyrazino[2,3-b] indole-2,3-dicarbonitrile (Cz4DPy) and 5-(3-(9H-carbazol-9-yl) pentyl)-5H-pyrazino[2,3-b] indole-2,3-dicarbonitrile (Cz5DPy) were synthesized via three step reactions as shown in Schemes S1–S3 (Supporting Information). Synthesized compounds were characterized by  $^1\text{H}$  and  $^{13}\text{C}$  NMR spectroscopy, high-resolution mass spectrometry (HRMS) (Figures S1–S22, Supporting Information), and X-ray single crystal X-ray diffraction structures. The purity of compounds was checked with high-performance liquid chromatography (HPLC) (Figure S23, Supporting Information). **Scheme 1** shows the schematic diagram of these multifunctional TSCT luminogens.

### 2.1. Single Crystal Structure Analysis and Supramolecular Interactions

To gain a better understanding of their structure-property relationship as well as the relationship between emission behaviors and intermolecular interactions, single-crystal X-ray diffraction (SC-XRD) was performed. While Cz2DPy, Cz3DPy, and Cz5DPy were successfully detected, crystals of Cz4DPy were not suitable enough to be perceived by X-ray crystallography. From their crystal structures, it was clearly observed that the different molecular configurations, Cz2DPy showed S-like architecture, however, Cz3DPy and Cz5DPy are in L and Z-shaped arrangements (**Figure 1A–C**). All molecules have planar donor and acceptor cores while their different length flexible alkyl chains are nearly perpendicular to their donor and acceptor moieties, impacting their molecular configurations and packing patterns. Cz3DPy shows more distorted geometry with a larger dihedral angle ( $\approx 73.06^\circ$ ) between the donor and acceptor units (**Figure S24A–C**, Supporting Information). With flexible alkyl chain increase from Cz2DPy to Cz5DPy, chromophores of carbazole and DIPy units exhibited well-distributed arrangements, especially for Cz5DPy with the longest alkyl chain. Subsequently, the intermolecular interactions in the crystals of Cz2DPy, Cz3DPy, and Cz5DPy (**Figure 1D–F**) were carefully studied. Numerous intermolecular interactions were observed in all the crystals, however, Cz5DPy exhibited the highest number of non-covalent intermolecular interactions. These intense intermolecular interactions help to rigidify the molecular conformation to activate the long lifetime of TADF for all the molecules and block the non-radiative pathway by restricting the molecular motions. For Cz2DPy, three numbers of C-H $\cdots\pi$  (2.808  $\text{\AA}$  – 2.826  $\text{\AA}$ ), two C-N $\cdots\text{H}$  (2.561–2.645  $\text{\AA}$ ) and one C-N $\cdots\pi$  (3.211  $\text{\AA}$ ) interactions are observed, whereas highly twisted structure Cz3DPy



**Scheme 1.** Chemical structures A) and schematic diagram B) of multifunctional TSCT luminogens, CznDPy ( $n = 2, 3, 4$ , and  $5$ ) with non-conjugated alkyl chains as a tuner. Where, “ $n$ ” represents the number of carbons in the alkyl chain, and the color of the leaf defines their respective emission behavior. Proposed Jablonski diagram C) of the emitters CznDPy ( $n = 2, 4$ , and  $5$ ) involving RISC from  $T_1$  ( $^3CT$ ) to  $S_1$  ( $^1CT$ ) and for Cz3DPy from  $T_2$  ( $^3LE+^3CT$ ) to  $S_1$  ( $^1CT$ ).

exhibited a lesser number of intermolecular interactions such as two numbers of C-H $\cdots\pi$  (2.887Å) and C-N $\cdots$ H (2.668Å-2.732Å) and one C-H $\cdots$ C-H (2.306Å). Comparatively a highest number of interactions (7) were found for Cz5DPy, two C-H $\cdots\pi$  (2.724Å – 2.895Å) and C-N $\cdots$ H ( $sp^3$ ) (2.58–2.60Å) interactions, one number of C–H $\cdots$ N (2.68Å), C–N $\cdots$ H (2.69Å), and C–H $\cdots$  C–H (2.36Å) interaction. In addition, two weak  $\pi\cdots\pi$  interactions (3.347 and

3.386 Å) between a donor moiety of one molecule to the acceptor of its neighboring molecule is observed for Cz5DPy which leads to the dimer formation, indicating a relatively flexible molecular packing mode (Figure 1F). All of them exhibit head-to-tail arrangements in their bulk packing. Cz2DPy with an even alkyl chain displays more ordered, symmetrical, and tight packing as compared to the odd alkyl chain containing Cz3DPy and Cz5DPy.

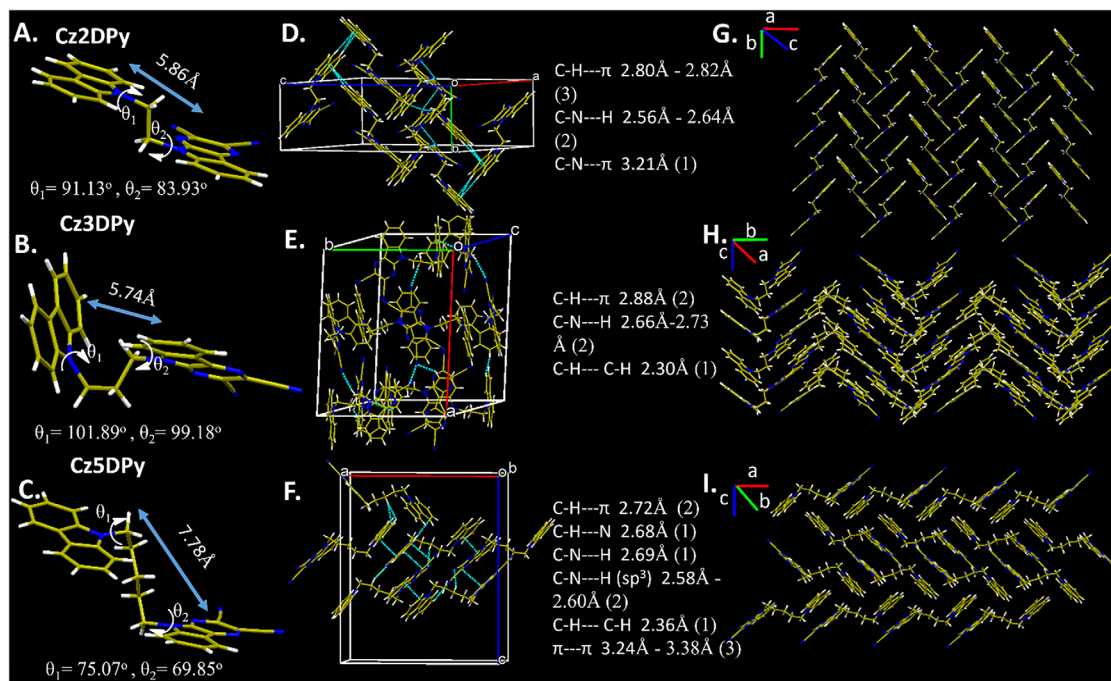


**Figure 1.** SC-XRD analysis: Configurations of Cz2DPy A), Cz3DPy B), and Cz5DPy C) from SCXRD. D, E, F) Intermolecular interactions and packing G, H, I) of Cz2DPy, Cz3DPy, and Cz5DPy respectively in their crystal structure.

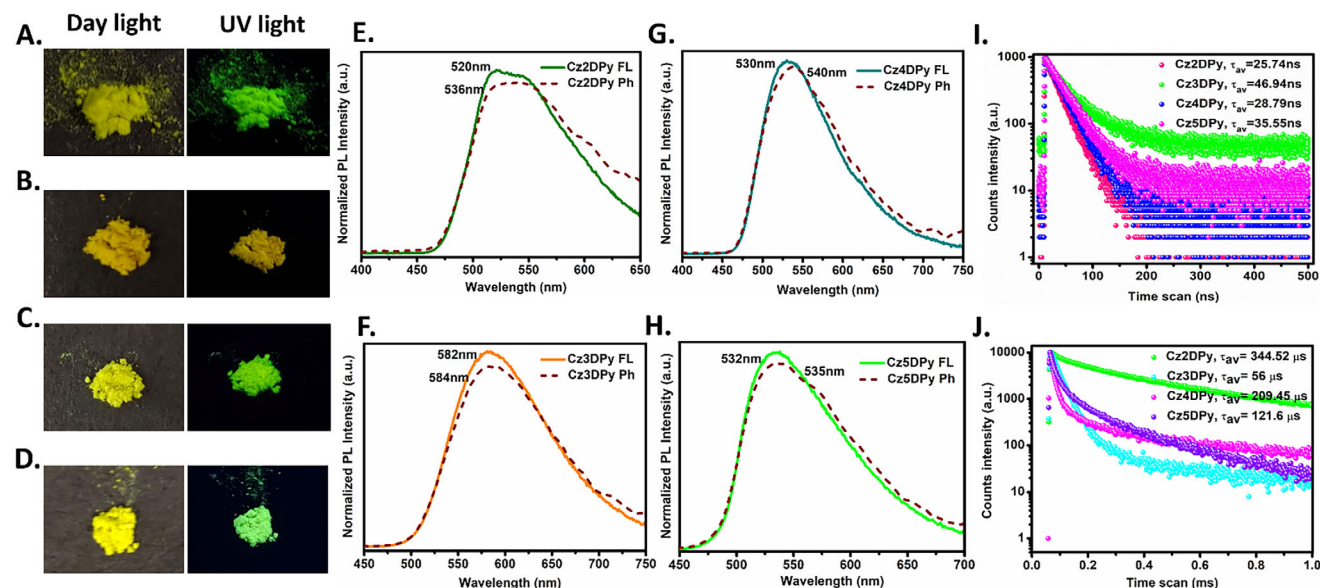


**Figure 2.** Solid-state optical properties: Photos of Cz2DPy (A), Cz3DPy (B), Cz4DPy (C), and Cz5DPy (D) under daylight and 365 nm UV light. E, F, G, H) Normalized fluorescence (solid line) and phosphorescence spectra (dotted line) of CznDPy ( $n = 2, 3, 4,$  and  $5$ ) in pristine powder form at 298K and their respective TRPL (I, J) decay profile (inset: average lifetime values were mentioned).

Systematic examination of structure-property relationships reveals that one of the leading causes of the small  $\Delta E_{\text{ST}}$  is the varying steric hindrance induced by their structural variation. Also, these numerous noncovalent interactions demonstrate the essentiality of alkyl chain regulation. PXRD analysis was carried out to ascribe their degree of crystalline nature variation at variable alkyl chains. This analysis exhibited sharp and intense multiple diffractions, revealing their microcrystalline nature (Figure S25, Supporting Information). Notably, the longer alkyl chain Cz4DPy and Cz5DPy showed a large number of sharp diffraction peaks in the low  $d$ -spacing region ( $2\theta$ ,  $20\text{--}30^\circ$ ) corresponding to the presence of more numbers of noncovalent interactions in their crystal structures. Overall, these studies display their denser noncovalent interactions and solid-state packing nature which is responsible for their multi-emissive nature.

## 2.2. Photophysical Properties

The photophysical properties of the synthesized compounds were thoroughly investigated in both the solution and solid states. The absorption spectra of these molecules in dilute DMF ( $30\ \mu\text{M}$ ) were nearly consistent with peaks at 280 and 345 nm (Figure S26, Supporting Information) which resulted in the  $\pi\text{-}\pi^*$  transition and intramolecular charge transfer (ICT) from carbazole (Cz) to dicyanoindolopyrazine (DIPy) moiety, respectively. Steady-state PL spectra of these compounds from Cz2DPy to Cz5DPy showed emission peaks at 435, 395, 393, and 390 nm in solution, which might be attributed to locally excited (LE) states (Figure S27, Supporting Information). Another emission band at  $\approx 508$  and 512 nm for Cz3DPy and Cz5DPy are assigned to TSCT states, respectively.

In the solid state, as the alkyl length increased from Cz2DPy to Cz5DPy, they exhibited green, orange, light green, and greenish-

yellow emission under 365 nm excitation (Figure 2A–D). They showed PL peaks at 515, 561, 523, and 525 nm (Figure 2E,G,F,H, solid lines) with prompt fluorescence lifetime values of 25.74, 46.94, 28.79, and 35.55 ns, respectively (Figure 2I) Cz3DPy exhibits a large stoke-shifted emission, which may be due to its most twisted steric conformer, which leads to its loose crystal packing structure that allows for greater freedom in the relaxation of excited states. Their phosphorescence spectra (Figure 2E,G,F,H, red dotted lines) show prominent broad, red-shifted emissions compared to their fluorescence spectra at 536, 584, 540, and 535 nm with delayed lifetime values of 344, 56, 209, and 121  $\mu\text{s}$  under ambient conditions (Figure 2J). Temperature-dependent studies (Figure S28, Supporting Information) further confirmed their delayed emission nature as TADF. Both lifetimes and emission intensity increased with increasing temperature. The absolute quantum yield for prompt fluorescence,  $\phi_{\text{PF}}$  and TADF quantum yield,  $\phi_{\text{DF}}$  of all the CznDPy powders were found to be 0.48, 0.18, 0.39, 0.32 and 0.37, 0.18, 0.30, 0.28 respectively. Further, rate constants of ISC ( $k_{\text{ISC}}$ ) and RISC ( $k_{\text{RISC}}$ ) were calculated from their quantum yields and lifetimes, estimated as  $2 \times 10^7$  and  $0.43 \times 10^4\ \text{s}^{-1}$  for Cz2DPy,  $1.7 \times 10^7$  and  $2.19 \times 10^4\ \text{s}^{-1}$  for Cz3DPy,  $2.12 \times 10^7$  and  $0.63 \times 10^4\ \text{s}^{-1}$  for Cz4DPy,  $1.9 \times 10^7$  and  $1.1 \times 10^4\ \text{s}^{-1}$  for Cz5DPy. Their emission wavelength, lifetime, and PLQY values vary due to the different molecular configurations, packing, and steric factors in the integrated TSCT systems. The nearly orthogonal and slightly twisted structures of Cz3DPy and Cz5DPy induce a faster rate of the RISC process ( $k_{\text{RISC}}$ ), resulting in shorter delayed lifetimes than Cz2DPy and Cz4DPy. In contrast, higher quantum efficiency and longer lifetimes of Cz2DPy and Cz4DPy can be attributed to their nearly linear configurations with compact symmetrical packing.

To explore the effect of the alkyl groups, the UV-vis absorption spectra were recorded in an aggregated state (Figure S29, Supporting Information). DMF and water were chosen as good

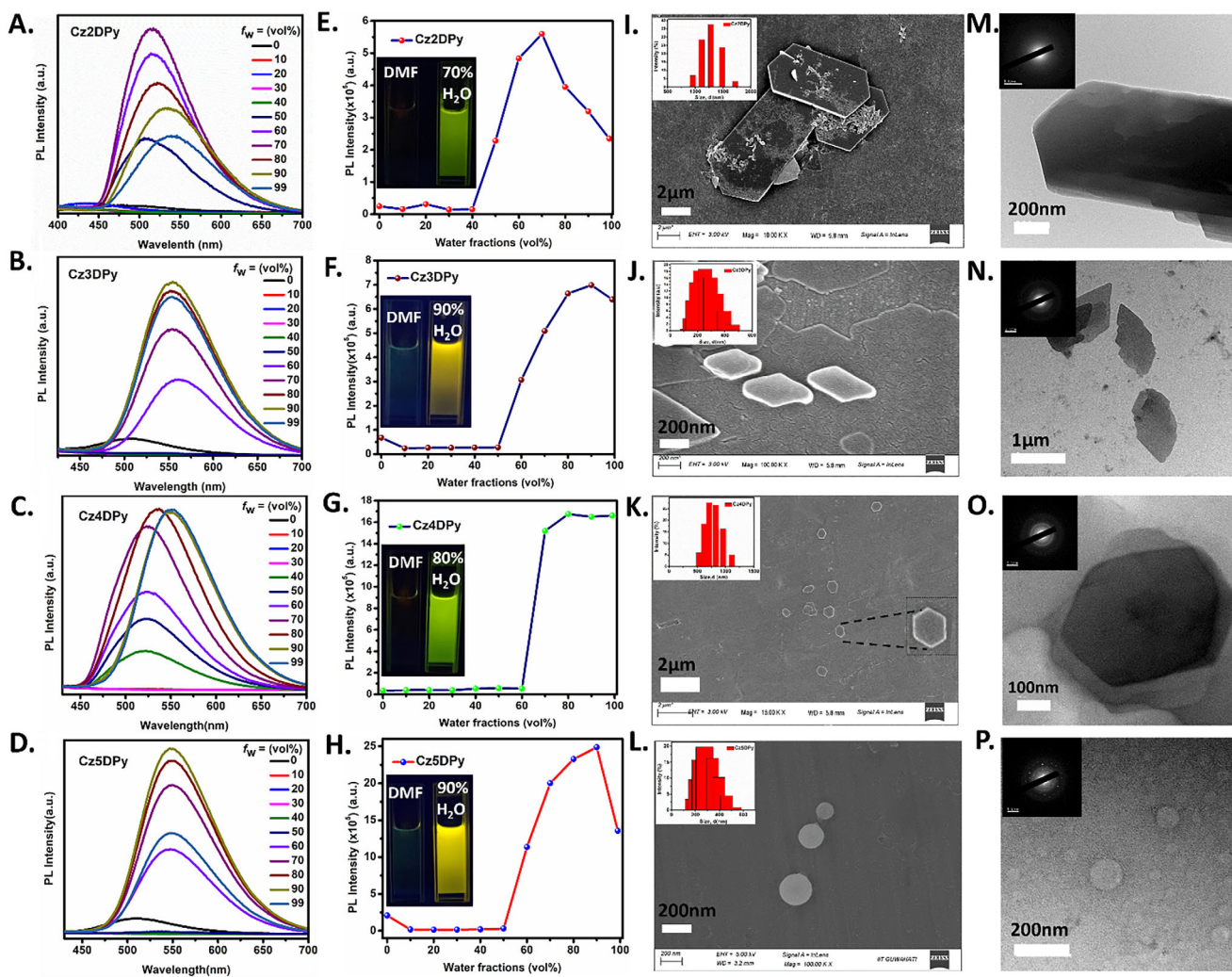


**Figure 3.** Aggregated state properties: A,B,C,D) PL spectra in DMF/water mixtures with different water fractions ( $\lambda_{\text{exc}} = 345$  nm). E,F,G,H) AIE curves with different DMF/water fractions (inset: photos were taken under 365 nm UV lamp). I,J,K,L) FESEM images (inset: DLS). M,N,O,P) TEM images (inset: SAED pattern) of Cz2DPy, Cz3DPy, Cz4DPy, and Cz5DPy in their aggregated state.

and poor solvents, hence their aggregated state emission properties were recorded in a DMF/water mixture. As shown in Figure S29 (Supporting Information), it is observed that the Cz2DPy and its three derivatives display analogical UV-vis absorption spectra in aggregated state at maximum wavelength of  $\approx 350$  nm, which is because of their homologous molecular structures and electronic properties.<sup>[13]</sup> To explore their AIE properties, we measured their fluorescence spectra in DMF/water mixtures at different water fractions (Figure 3A–D for Cz2DPy, Cz3DPy, Cz4DPy, and Cz5DPy, respectively). Interestingly, all of the emitters exhibited good AIE properties at the various water fractions of 70% to 99% (Figure 3E–H; Figure S30, Supporting Information). Notably, when the length of alkyl chains increases from ethyl to pentyl, AIE-effect becomes more pronounced, possibly due to the restrictions of molecular motions and vibrations, including extensive non-covalent interactions at the higher water fractions. The non-radiative excited state decay is blocked in the aggregated state, which enables the molecules to emit strongly. In their aggregated states, odd alkyl chains containing Cz3DPy and

Cz5DPy exhibit a more pronounced, red-shifted emission (yellow) than Cz2DPy and Cz4DPy, which emit a green color. The greater Stokes shifts of Cz3DPy and Cz5DPy can be attributed to their twisted conformations, which reduce the electronic coupling between the donor and acceptor moieties, as well as their loose crystal packing which permits a more substantial relaxation of the excited state. We further confirmed their aggregation nature via different shape and sizes of micro and nanoparticles with DLS, FESEM (Figure 3I–L), and FETEM studies (Figure 3M–P). All of them have different morphologies in their aggregation state where Cz2DPy and Cz4DPy form hexagonal-shaped microaggregates and nano aggregates with an average size of 1300 and 700 nm, on the other hand, Cz3DPy and Cz5DPy forms diamond and round shaped nano aggregates with 250 nm average size in their respective FESEM and FETEM images. The differences in the size of their aggregates can be due to their distinct steric hindrance and molecular packing caused by the different alkyl chains. The formation of larger aggregates by molecules with even alkyl chains can be ascribed to their highly ordered and

**Table 1.** Photophysical properties of CznDPy.

Emitters	$\lambda_{\text{abs}}^{\text{a)}$ [nm]	$\lambda_{\text{PF}}^{\text{b)}$ [nm]	$\lambda_{\text{DF}}^{\text{c)}$ [nm]	$\lambda_{\text{DF}}^{\text{c)}$ [nm]	$\tau_{\text{PF}}^{\text{b)}$ [ns]	$\tau_{\text{PF}}^{\text{c)}$ [ns]	$\tau_{\text{DF}}^{\text{c)}$ [ $\mu\text{s}$ ]	$\Phi_{\text{PF}}^{\text{c)}$	$\Phi_{\text{DF}}^{\text{c)}$	$k_{\text{ISC}}^{\text{c)}$ [ $\times 10^7 \text{ s}^{-1}$ ], $k_{\text{RISC}}^{\text{c)}$ [ $\times 10^4 \text{ s}^{-1}$ ]	$\Delta E_{\text{ST}}$ [eV]
Cz2DPy	345	515	520	536	23.27	25.74	344	0.48	0.37	2.0, 0.43	0.03
Cz3DPy	345	555	582	584	34.68	46.94	56	0.18	0.18	1.7, 2.19	0.02
Cz4DPy	345	535	530	540	27.23	28.79	209	0.39	0.30	2.12, 0.63	0.004
Cz5DPy	345	552	532	535	48.86	35.55	121	0.32	0.28	1.9, 1.1	0.0003

Abs = Absorbance, PF = Prompt fluorescence, DF = Delayed fluorescence,  $\Phi$  = Quantum yield. <sup>a)</sup> Measured in DMF (30  $\mu\text{M}$ ); <sup>b)</sup> Measured in aqueous (aggregated) state; <sup>c)</sup> Measured in solid (powder).

densely packed structure in the aggregated state, supported by their linear conformation. In contrast, the odd-chain molecules, which have twisted structures, exhibit less ordered and relatively loose packing in the aggregated state, resulting in smaller aggregates.<sup>[14]</sup> SAED patterns (FETEM) showed that the nanoaggregates of Cz5DPy are crystalline in nature compared to the amorphous nature of Cz2DPy, Cz3DPy, and Cz4DPy aggregates (inset: Figure 3M–P). Longer alkyl chain molecules Cz4DPy and Cz5DPy exhibit good AIE nature with high absolute quantum yields ( $\Phi_{\text{PF}}$ ) of 0.36 and 0.37 respectively, as compared to their shorter alkyl chain equivalents, which could be due to the formation of a more significant number noncovalent interactions in restricted geometry at their increasing alkyl chain lengths in the condensed state. Their AIE study shows that there is a pronounced odd-even effect of alkyl chains on their aggregation properties due to their different conformations and steric strain,<sup>[15]</sup> and their nano aggregation behavior increases with increasing hydrophobic alkyl chain lengths.<sup>[16]</sup> Their lifetimes in the aggregated state and DMF solution are recorded (Figure S31, Supporting Information) and a noticeable increment in lifetimes in their condensed state compared to the solution state as due to reduced non-radiative decay pathways was observed. Further, TADF studies in their aggregated state showed the delayed nature. New red shifted peaks were observed in their delayed emission spectra (Figure S32A, Supporting Information) with a lifetime of 134, 40, 87, and 79  $\mu\text{s}$  (Figure S32B, Supporting Information) and  $\Phi_{\text{DF}}$  of 0.09, 0.21, 0.33, and 0.29 respectively for CznDPy ( $n = 2, 3, 4,$  and 5). Thus, the presence of DF nature of all the emitters in their aggregated state denotes their aggregation-induced delayed fluorescence (AIDF) property. Detailed analysis of their photophysical properties is summarized in Table 1. To examine their intramolecular TSCT behavior we measured their absorption and fluorescence spectra in solvents with different polarities (Figures S33 and S34, Supporting Information). Though solvent had no effect on their absorption spectra, i.e., their ground state, it had a positive solvatochromism effect on their PL spectra, confirming their CT nature in the excited state.<sup>[17]</sup>

Both Cz2DPy and Cz4DPy showed a prominent bathochromic shift of CT peak with increasing solvent polarities up to 48 and 50 nm respectively. On the other hand, Cz3DPy and Cz5DPy showed a small bathochromic shift of CT peak with 20 and 30 nm, confirming their comparatively less CT nature. Unlike for Cz5DPy, in high-polar solvents like DMF and acetonitrile, their CT peak got diminished due to the stabilization of the CT state in high-polar solvents. For Cz5DPy, due to the presence of longer alkyl spacer group CT from donor to acceptor is decreased, and therefore their CT state is not that stabilized in high polar sol-

vents. The good CT nature of Cz2DPy and Cz4DPy can be attributed to their linear structures (Figure S34A,C, Supporting Information) with proper orbital alignment, which helps in electronic coupling between the donor and acceptor for CT. In contrast, the twisted structures (Figure S34B,D, Supporting Information) of Cz3DPy and Cz5DPy can alter the spatial orientation of the molecular orbitals in the donor and acceptor moieties, making their alignment less favorable for efficient CT. The misalignment of these orbitals reduces their overlap, thereby limiting the donor-acceptor electronic coupling. Cz3DPy exhibits the lowest CT nature due to the most twisted conformation.<sup>[18]</sup> The degree of CT was further determined by measuring the intensity of CT emission and absorption (at 345 nm), which clearly showed an odd-even effect.<sup>[19]</sup> The CT emission and absorption intensities in CznDPy ( $n = 2$  and 4) were notably stronger than in CznDPy ( $n = 3$  and 5), indicating enhanced CT in the exciplex systems with even alkyl chains (Figure S35, Supporting Information). These findings demonstrated that CznDPy ( $n = 2, 3, 4,$  and 5) has ICT and AIE properties and suggest that the alkyl substituent effect plays a vital role in regulating molecular packing.

### 2.3. Computational Results

To explore the mechanism of TADF behavior, DFT and TD-DFT calculations were performed based on optimized single crystal structure at the B3LYP/6-31G (d, p) level (Figure S33, Supporting Information). Cz2DPy and Cz4DPy display nearly linear configurations, whereas Cz3DPy and Cz5DPy exhibit a twisted conformation, demonstrating that alkyl linkers have an odd-even influence on molecular geometries. For all of them, HOMO is mainly distributed on carbazole (donor) and LUMO is on the DIPy moiety (acceptor), which gives a well-separated HOMO-LUMO (Figure 4A,B; Figure S38A,B, Supporting Information). To understand the nature of CT between donor and acceptor, HOMO-LUMO distribution was also carried out in their dimer state (Figure S37, Supporting Information). For all of them, the HOMO and LUMO were located on the same molecule, indicating that intramolecular CT is responsible for its TSCT nature. This may be due to the flexible nature of alkyl chains that allows some orbital overlap between donor and acceptor to facilitate intramolecular CT.<sup>[20]</sup>

Although alkyl chain length has no significant effect on their HOMO-LUMO energies, with chain length increasing from Cz2DPy to Cz5DPy, HOMO-LUMO separation is well distinguished and the  $\Delta E_{\text{ST}}$  value decreased from 0.03 to 0.0003 eV suggesting the prospect for rapid equilibration of the  $T_1$  ( $T_2$  for Cz3DPy) and  $S_1$  states. As the length of the spacer group

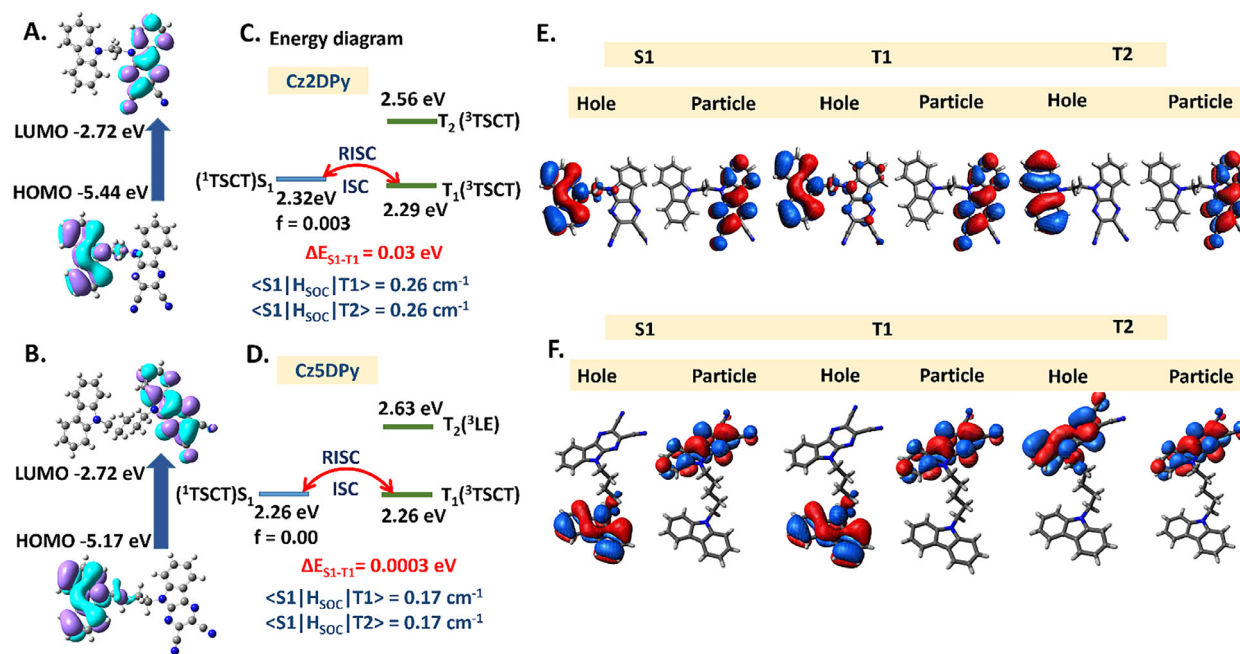


**Figure 4.** Theoretical calculations (DFT/TD-DFT): A,B) HOMO-LUMO distributions, C,D) energy states and E,F) the active natural transition orbitals (NTOs) of Cz2DPy and Cz5DPy respectively using B3LYP/6-31G (d, p) level of study.

increases, there will be less electron density overlap between HOMO and LUMO, giving small exchange integral value ( $J$ ) and  $\Delta E_{ST}$ . These small  $\Delta E_{ST}$  ( $\leq 0.5$  eV) values induce the RISC process and boost the TADF phenomenon. As RISC occurs between two close energy value states, for Cz2DPy, Cz4DPy, and Cz5DPy RISC will be from  $T_1$  (2.29, 2.43, and 2.26 eV) to  $S_1$  (2.32, 2.43, and 2.26 eV) state (Figure 4C,D; Figure S38D, Supporting Information). On the other hand, for Cz3DPy  $T_2$  (2.72 eV) has similar energy with  $S_1$  (2.70 eV) so RISC will happen from  $T_2$  to  $S_1$  (Figure S38C, Supporting Information). To know the nature of their singlet and triplet states, natural transition orbital (NTO) analyses were done up to three states, i.e., for  $S_1$ ,  $S_2$ ,  $S_3$ ,  $T_1$ ,  $T_2$ , and  $T_3$  (Tables S1–S8, Supporting Information). For Cz2DPy, Cz4DPy, and Cz5DPy,  $S_1$  and  $T_1$  states are showing CT nature (Figure 4E,F; Figure S38F, Supporting Information). However, for Cz3DPy,  $S_1$  has CT character and  $T_1/T_2$  exhibits a mixed character of LE and CT, i.e., hybridized localized CT (HLCT) state (Figure S38E, Supporting Information). Both twisted configuration and HLCT nature of  $T_2$  state fasten the RISC process in Cz3DPy, showing the shortest delayed lifetime among them (Figure 2J).<sup>[21]</sup> Since all the molecule's charge transfer mode is through space instead of through bonds, we denoted the CT state as TSCT.<sup>[22]</sup>

From these findings, we can conclude that for Cz2DPy, Cz4DPy, and Cz5DPy, the  $^1CT$  ( $S_1$ ) and  $^3CT$  ( $T_1$ ) states will be involved in the RISC process, whereas for Cz3DPy, which has a more contorted structure with dihedral angle of  $73.06^\circ$ ,  $^1CT$  ( $S_1$ ) and  $^3HLCT$  ( $T_2$ ) states will be involved in RISC. These energy diagrams favor all the molecules' TSCT TADF natures (Figure 4; Figure S38, Supporting Information). Spin-orbit coupling matrix element (SOCME) values between  $S_1$  and  $T_1$ ,  $T_2$ , and  $T_3$  states are calculated for all emitters (Table S9, Supporting Information). The SOCME of Cz3DPy between  $S_1$  ( $^1CT$ ) and  $T_2$  ( $^3HLCT$ ) is

larger than that of other emitters with only CT nature, indicating relatively strong SOC between different spatial orbital occupations ( $^1CT$  and  $^3LE$ ) according to El-Sayed's rule.<sup>[23]</sup>

To gain theoretical insights into their intramolecular non-covalent interactions, reduced gradient density (RDG) analysis, and isosurfaces were performed with the TD-DFT geometry and Multiwfn software (Figure S39A,B, Supporting Information). RDG analysis confirms the presence of non-covalent interactions (green region) and steric hindrance (brown color) between donor and acceptor (Figure S39A, Supporting Information). It can be observed from RDG isosurfaces (Figure S39B, Supporting Information) that the noncovalent interactions exist mainly between the  $-CH_2$  groups of alkyl chains and the donor and acceptor moieties.<sup>[18]</sup> As the alkyl chain length increases from Cz2DPy to Cz5DPy, intramolecular interactions dominate over steric hindrance as alkyl chains will provide space between the D and A. These intramolecular interactions will restrict their intramolecular vibrations and prohibit the non-radiative pathways to achieve efficient emissive behavior in solid state.

#### 2.4. Mechanoluminescence (ML) and Mechanochromism (MC)

Upon mechanical grinding, all of them showed emission-switching behavior due to the presence of flexible alkyl chains and different kinds of intra/intermolecular interactions. Short alkyl chains containing Cz2DPy and Cz3DPy exhibit reversible ML while Cz4DPy and Cz5DPy with longer chains show reversible MC behavior upon mechanical force and fumigation with DCM vapor, respectively. We examine their ML and MC behavior with PL spectra, PXRD, DSC, and TGA analysis. Cz2DPy and Cz3DPy display ML spectra at 515 and 560 nm, and after fuming with DCM (dichloromethane) vapor it resumes its

original state (Figure S40B,E, Supporting Information). The PL emission enhancement for Cz2DPy and Cz3DPy was favorably influenced by their strong molecular rigidity, which is confirmed from their PXRD analysis. After grinding, their diffraction peaks in the region of 20°–30° were still sharp and strong in different states (pristine, grinding, and solvent fuming) (Figure S40C,F, Supporting Information). Some new peaks can also be observed for Cz3DPy, which shows their strong robustness and ML (Figure S40F, Supporting Information). On the other hand, Cz4DPy and Cz5DPy with a long and more flexible alkyl chain showed MC with a red shift of 33 and 18 nm after grinding, respectively (Figure S40H,K, Supporting Information) and can be restored to their emission by DCM fuming for multiple cycles (Figures S41,S42, Supporting Information). The shifting of emission maxima of these luminogens after grinding was attributed to a variation in the crystalline degree, which is evidenced by their PXRD analysis in Figure S40I,L (Supporting Information). After grinding, their diffraction peaks almost disappeared which is retrieved after DCM fuming. The presence of a more significant number of sharp diffraction peaks ( $2\theta$ , 20°–30°) for Cz4DPy and Cz5DPy can be attributed to the greater number of non-covalent interactions, therefore upon mechanical grinding, there will be more alterations of their non-covalent interactions which results in MC.<sup>[24]</sup> Cz4DPy exhibits more sharp diffraction peaks in that region, which deduces a greater number of non-covalent interactions and a high degree of crystallinity nature, thus upon grinding an unusual and more pronounced MC behavior is observed in Cz4DPy in comparison to Cz5DPy. Differential scanning calorimetry (DSC) was also performed for Cz3DPy, Cz4DPy, and Cz5DPy to know their phase transition behavior upon grinding (Figures S43–S45, Supporting Information). DSC results showed different endothermic phase transitions (melting) at 230 °C, 266 °C, and 219 °C for Cz3DPy, Cz4DPy, and Cz5DPy before and after grinding. An exothermic crystalline phase transition is shifted from 170 °C to 158 °C for Cz3DPy. Exothermic crystalline phase transition of pristine Cz4DPy shows a sharp, intense peak at 254 °C but after grinding, it gives a little shifted peak at 248 °C, which demonstrated that the grinding partially destroyed the crystals and converted them to an amorphous state.<sup>[25]</sup> For Cz5DPy, the pristine powder exhibited a sharp endothermic peak at 219 °C, confirming its highly ordered structure. Upon grinding, the peak broadened, and a new exothermic peak emerged at 169 °C, indicating a phase transition from an ordered to a disordered state.<sup>[26]</sup> Similarly, thermogravimetric analysis (TGA) supported the observed phase transition in the MCL phenomenon for Cz4DPy and Cz5DPy (Figures S46,S47, Supporting Information). The analysis revealed differences in the degradation temperatures between the pristine and ground samples. The pristine samples exhibited higher thermal stability compared to the ground ones, due to the phase transition from a crystalline to an amorphous state. For Cz4DPy, the degradation temperature decreased from 406 °C to 363 °C after grinding, while Cz5DPy showed a decrease from 384 °C to 344 °C. Therefore, we deduced that the flexible alkyl chain regulates the spectral shift in response to an external force.

TGA analysis shows that all molecules have thermal stability up to  $\approx$ 400 °C. However, a slight weight loss is observed for Cz3DPy and Cz5DPy  $\approx$ 200 °C (Figure S48, Supporting Information). We observed a correlation between the decomposition tem-

perature and the odd-even alkyl chain pattern of the molecules. Cz2DPy and Cz4DPy, which have even alkyl chains, are more thermally stable than Cz3DPy and Cz5DPy, which have odd alkyl chains. This difference in thermal stability could be attributed to the former molecules' greater molecular symmetry.<sup>[27]</sup> Additionally, the presence of twisted configurations and long flexible alkyl chains contribute to the decreased thermal stability of Cz3DPy and Cz5DPy, respectively.

## 2.5. Cellular Toxicity Study

Considering the potential therapeutic applications of the compounds with AIDF behavior, the biocompatibility and the cellular toxicity of the compounds were assessed. The cell viability was assessed by MTT assay on human breast cancer cell line MDA-MB-231 and human glioblastoma cell line U87MG (Figure S49, Supporting Information). These cell lines were selected due to their relevance in cancer research and their distinct biological characteristics. The cells were treated with varying concentrations of compounds ranging from 5 to 100  $\mu$ M to evaluate the dose-dependent cytotoxicity. The MTT assay disclosed that the compounds maintained good cell viability even at higher concentrations of 75  $\mu$ M in both the cell lines suggesting their low cytotoxicity and good cellular tolerance. The U87MG cells were more sensitive to the compounds than the MDA-MB-231 cells suggesting cell line-specific response which may be due to differences in metabolic activity of the cells. The minimal cytotoxic effects suggest that these compounds can be used as effective imaging agents.

## 2.6. Photostability Study

To measure the photostability of all the synthesized compounds, UV-vis absorption, and emission intensities were measured with the continuous irradiation of xenon light for 40 with 5 min of interval time (Figures S50,S51, Supporting Information). For comparison, we included three standard imaging agents, propidium iodide (PI), 4',6-diamidino-2-phenylindole (DAPI), and Rhodamine 6G (R6G), and evaluated their photostability under the same condition. Remarkably, all the synthesized compounds demonstrated good photostability, showing no significant reduction in absorbance or emission intensities during continuous light exposure. Furthermore, these compounds exhibited significantly higher photostability compared to PI, DAPI and R6G. The absorbance of all the synthesized compounds remained above 96% of the original value, while the absorbance of PI, DAPI, and R6G dropped to 55%, 70%, and 86%, respectively, after the same irradiation time. For fluorescence intensity, Cz $n$ DPy ( $n = 2, 3, 4,$  and 5) decreased to  $\approx$ 93% after 40 min of continuous irradiation, while PI and DAPI were bleached to 79% and 90%, respectively. The emission of R6G shifted from 616 to 605 nm without affecting its intensity. Furthermore, Cz2DPy was used for imaging human breast cancer cell lines MDA-MB-231 under continuous irradiation with a 405 nm laser for 15 min with 3 min intervals (Figure S52, Supporting Information). For comparison, PI dye was tested under the same conditions. The fluorescence intensity of Cz2DPy showed minimal change, while there was a significant

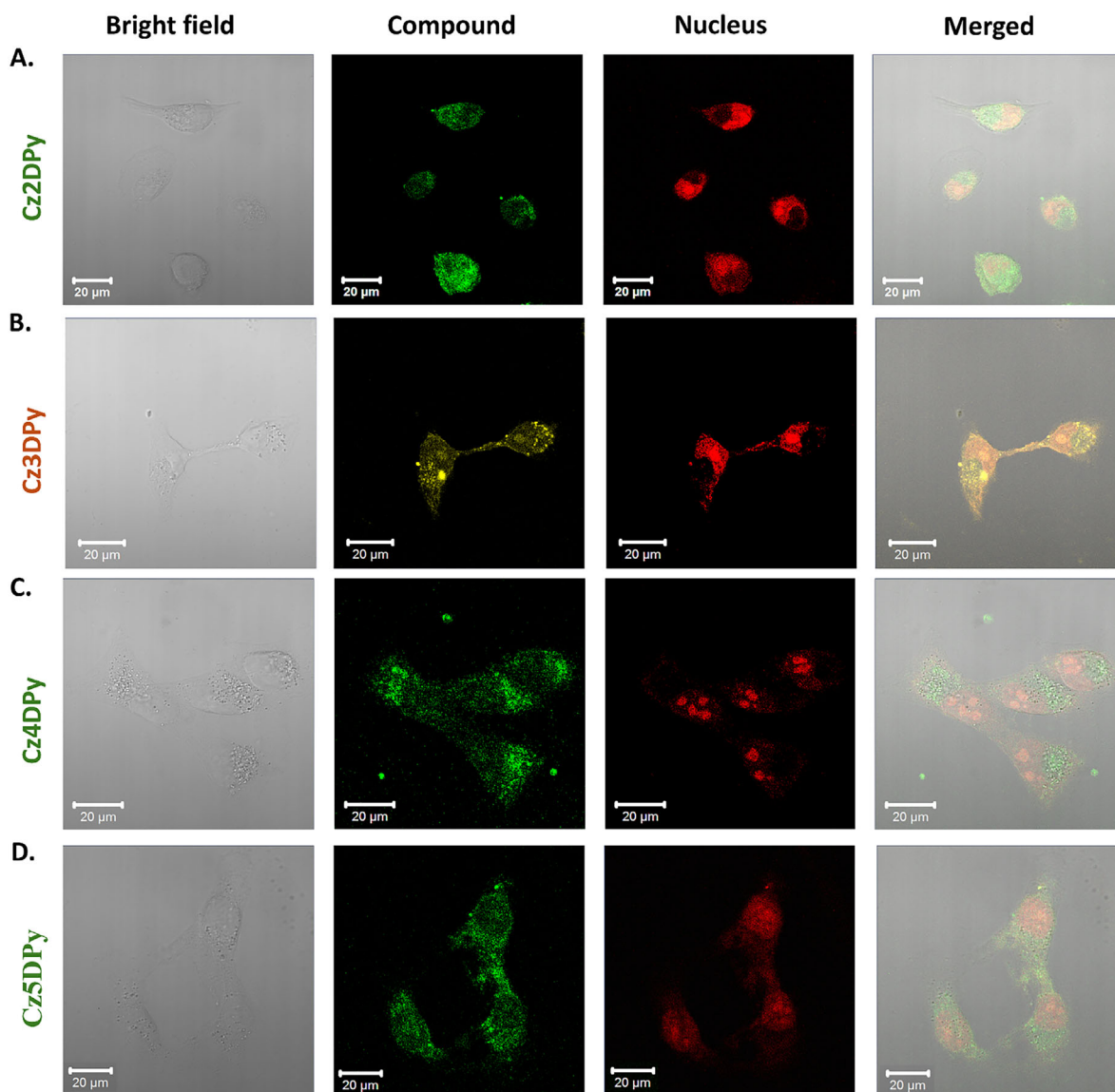


**Figure 5.** Imaging: Confocal images of MDA-MB-231 cancer cells incubated with  $10 \mu\text{g mL}^{-1}$  Cz2,3,4,5DPy for 6 h; were collected using 405 and 561 nm lasers as excitation sources between 500 and 600 nm. All images are in 20  $\mu\text{m}$  scale bar. Results in A,B,C, and D) are replicated independently four times with persistent outcomes.

decrease in fluorescence intensity for PI after 15 min of continuous laser irradiation. These results indicate the remarkable photostability nature of all the luminophores suitable for long-term imaging applications.

### 2.7. Cellular Internalization, Localization, and Long-Term Imaging Studies

Given that the Cz2DPy, Cz3DPy, Cz4DPy, and Cz5DPy showed low cytotoxicity, the internalization and subcellular localization were assessed by confocal laser scanning microscopy (CLSM). The MDA-MB-231 were incubated with each of the compounds at a concentration of  $10 \mu\text{M}$ , a dose confirmed to be non-toxic, and cells were counterstained with propidium iodide (PI) to label

the nuclei. CLSM revealed effective internalization of the compounds, as evidenced by green fluorescence for Cz2DPy, Cz4DPy, and Cz5DPy, and yellow fluorescence for Cz3DPy (Figure 5). The PI staining indicated that the compounds were localized predominantly in the cytoplasm, confirming successful uptake and cytoplasmic accumulation. High signal-to-noise ratio (SNR) values of 431 for Cz2DPy, 719 for Cz3DPy, 144 for Cz4DPy, and 120 for Cz5DPy indicate their potential for high-resolution bioimaging with minimal autofluorescence interference (Figure S53, Supporting Information). To assess the long-term imaging capability of the compounds, imaging was performed after seven days of incubation with Cz2DPy and Cz3DPy. There was no notable change in the emission intensity of these compounds even after this extended period (Figure S54, Supporting Information), signifying their exceptional photostability and

resistance to photobleaching. This sustained fluorescence indicates their potential for long-term bioimaging applications, allowing for prolonged observation of cellular dynamics and response to treatments.

## 2.8. Cellular Uptake Mechanism Study

To understand the mechanisms of cellular internalization of the compounds, the fluorescence intensity of the internalized molecules was determined in the presence of inhibitors such as sodium azide (ATPase inhibitor), dynasore (dynamin inhibitor), phenothiazine, chlorpromazine (clathrin-mediated endocytosis inhibitor) and methyl- $\beta$ -cyclodextrin (caveolin-dependent endocytosis inhibitor). The results indicate that the internalization of Cz2DPy, Cz4DPy, and Cz5DPy is an active and energy-dependent process. The uptake was significantly reduced by treatment with dynasore, phenothiazine, and chlorpromazine, indicating the involvement of clathrin-mediated endocytosis. Methyl- $\beta$ -cyclodextrin treatment significantly downregulated the uptake of Cz2DPy and slightly affected Cz4DPy and Cz5DPy, suggesting that Cz2DPy also utilizes caveolin-mediated endocytosis. This data confirms that Cz2DPy internalization depends on both clathrin- and caveolin-mediated pathways, whereas Cz4DPy and Cz5DPy predominantly utilize clathrin-mediated endocytosis (Figure S55, Supporting Information). In contrast, the uptake of Cz3DPy was unaffected by any of the inhibitors tested, indicating that its internalization might occur through passive diffusion rather than active transport mechanisms. The presence of these compounds within the cytoplasm of the cells confirms their internalization and suggests that they utilize active cellular processes for internalization. To explore the influence of compound concentration and incubation time on clathrin- and caveolin-mediated pathways, a cellular uptake study of Cz2DPy and Cz3DPy in MDA-MB-231 cells was performed at concentrations of 5, 25, and 50  $\mu\text{M}$  (Figure S56A,B, Supporting Information) and incubation times of 2, 6, 12, and 24 h (Figure S56C,D, Supporting Information) in the presence of the respective inhibitors. At higher concentrations, Cz2DPy uptake decreased overall in the presence of inhibitors, while Cz3DPy uptake was unaffected as it was mediated by simple diffusion. The study demonstrates that small structural variations in the compounds lead to significant differences in their properties and cellular uptake pathways. Further, understanding the distinct internalization pathways is important for the design of targeted drug delivery systems and advanced bioimaging agents. Tailoring the structures of the compounds to exploit specific endocytic routes can enhance the specificity and efficiency of cellular uptake, and improve the efficacy of therapeutic agents and fluorescent probes. This has significant implications for developing treatments that require targeted delivery to specific cell types or intracellular compartments. In addition, the endocytic pathways are altered during diseases, and compounds that specifically use the altered endocytic pathways can be developed for targeted personalized therapy.

## 3. Conclusion

In summary, we have successfully synthesized a series of four novel TSCT materials designated as CznDPy ( $n = 2, 3, 4$ , and

5) that exhibited AIE, TADF, AIDF, ML, and MC properties simultaneously. To the best of our knowledge, these are the first examples consisting of novel acceptor moiety and even-odd alkyl chain modulated D- $\sigma$ -A small type pure organic molecules with adjustable TSCT, AIE, TADF, AIDF, ML, and MCL features with low  $\Delta E_{\text{ST}}$  values (0.03–0.0003 eV), longer lifetimes (56 to 344  $\mu\text{s}$ ) and higher total quantum efficiency (36–85%) making them highly effective for long term bioimaging of cancer cells. Notably, the odd alkyl chain containing Cz3DPy and Cz5DPy exhibited twisted structures with loose packing, which accelerates the RISC process resulting in a shorter TADF lifetime and lower quantum efficiency compared to even alkyl chains containing Cz2DPy and Cz4DPy, which have more linear systems and compact packing. HLCT nature further promotes the RISC process for the most twisted molecule, Cz3DPy, which has the shortest lifetime. Cz2DPy and Cz3DPy, which have shorter alkyl chains, exhibit ML due to their robust nature, whereas Cz4DPy and Cz5DPy exhibit MC due to their crystalline-to-amorphous phase transition upon mechanical grinding. With their remarkable AIDF property in their aqueous solution, we successfully used them for efficient and prolonged imaging of human breast cancer cells MDA-MB-231. This study provided very intrinsic insights into the relationship between the odd-even effect of the alkyl chain on the molecular structure and properties of multifunctional TSCT TADF materials and their proficient bioimaging as well as internalization mechanisms, paving the way for the customization of the unusual photophysical behavior, cellular uptake pathways and the development of targeted personalized therapeutic applications.

## 4. Experimental Section

**Materials:** Isatin, diaminomaleonitrile, carbazole (purified by column chromatography), 1,2-dibromoethane, 1,3-dibromopropane, 1,4-dibromobutane, 1,5-dibromopentane, p-toluenesulfonic acid, potassium hydroxide, and potassium carbonate were purchased from Sigma-Aldrich and used as received. Solvents such as 1,4-dioxane, acetone, and dimethylformamide were purified following standard protocols and stored over molecular sieves.

**Preparation of CznDPy:** For the preparation of CznDPy series, 1 mmol of CznBr (Cz2Br = 300 mg, Cz3Br = 350 mg, Cz4DPy = 360 mg, and Cz5DPy = 370 mg), 1.1 mmol of 5H-pyrazino[2,3-b] indole-2,3-dicarbonitrile (400 mg) and 1.1 mmol of  $\text{K}_2\text{CO}_3$  (300 mg) were added to a 50 mL round-bottom flask with DMF (5 mL) solvent. The mixture was stirred at 90  $^\circ\text{C}$  for 8 h. Then  $\text{CH}_2\text{Cl}_2$  was added, and the organic phase was washed by water three times. The organic layer was dried over anhydrous  $\text{Na}_2\text{SO}_4$  and removed. The residue was purified by silica gel (100–200 mesh) with column chromatography using solvent (Hexane/dichloromethane 1.5:1 v/v; 1.22:1 v/v; 1:1 v/v with respect to polarity of the products) as the eluent to obtain a desired product (green for Cz2DPy, orange for Cz3DPy, yellowish green for Cz4DPy and Cz5DPy) with a yield of 85%.

**Measurements:** The  $^1\text{H}$  and  $^{13}\text{C}$  NMR spectra were recorded by using deuterated solvents ( $\text{CDCl}_3$  and  $\text{DMSO}-d_6$ ) in Bruker 600, 500, and 400 MHz NMR spectrometers. The absorption and fluorescence spectra were measured with PerkinElmer, Model Lambda-25 spectrometer, and Horiba-Fluoromax4 with Varian Cary Eclipse spectrometer respectively. The time-resolved fluorescence lifetimes were investigated with the time-resolved fluorescence studies were performed using an Edinburgh Life Spec II instrument. Temperature-dependent (150–298K) PL, lifetime measurements, and absolute quantum yields were carried out using a liquid nitrogen-cooled optical cryostat (Optistat, Oxford Instruments) and integrating a sphere attached to an Edinburgh FLS-1000 instrument. The morphology and crystallinity of CznDPy ( $n = 2, 3, 4$ , and 5) were examined

by scanning electron microscopy (FESEM) (Zeiss, Model: Sigma-300 and Gemini-300) and field emission transmission electron microscope (Jeol, Model:2100F). Single-crystal structures of Cz2DPy, Cz3DPy, and Cz5DPy were obtained on an X-ray diffractometer on Agilent and Bruker. All the crystal structures were solved by SHELXT with direct methods. The transition temperatures and associated enthalpy changes were determined by a differential scanning calorimeter (Q20 DSC) under a nitrogen atmosphere. Thermogravimetric analyses (TGA) were carried out with a Netzsch DSC/TGA analyzer in a temperature range of room temperature to 1200 °C under a nitrogen atmosphere at 5 °C min<sup>-1</sup> heating rate. For cell culture, MDA-MB-231 Breast Cancer cell line and U87MG Glioblastoma cell line were procured from the National Centre for Cell Science in Pune, India. MDA-MB-231 and U87MG cell lines were maintained using Dulbecco's Modified Eagle Medium (Gibco:12800-058) supplemented with 10% fetal bovine serum (FBS) and 1% penicillin and streptomycin antibiotics in a CO<sub>2</sub> incubator (5% CO<sub>2</sub> and 37 °C). Cellular imaging was performed using a confocal microscope in 63X with oil (CMSM, ZEISS LSM-880) with 408 nm laser as an excitation source.

**Theoretical Methods:** All DFT and TDDFT calculations in this study were performed by employing the combination of Becke3-Lee-Yang-Parr (B3LYP) hybrid functional and 6–31G (d, p) basis set using the Gaussian 16 package. The spin-orbit coupling matrix element (SOCME) was calculated using ORCA 5.0 at the B3LYP/DEF2-SVP level.

**Statistical Analysis:** The absorbance values were normalized to their respective control conditions, and blank readings were subtracted to account for autofluorescence. The validity of the data was tested by repeating the experiments ( $n = 4$  for S49, S55, and S56), and the values shown are Mean  $\pm$  SD. Statistical analysis was performed with Microsoft Excel and Student's *t*-test was used to compare between experimental groups, and *p* values < 0.05 were considered statistically significant.

## Supporting Information

Supporting Information is available from the Wiley Online Library or from the author.

## Acknowledgements

Financial grants from the Department of Science and Technology, New Delhi, India project no. DST/CRG/2019/002614, Deity, India no. 5(1)/2022-NANO, Indian Council of Medical Research (ICMR), Grant no. 5/3/8/20/2019-ITR and Max-Planck-Gesellschaft IGSTC/MPG/PG(PKI)/2011A/48 are acknowledged. The authors also thank the Param-Ishan supercomputing facility, Centre for Nanotechnology, Department of Chemistry (FIST: SR/FST/CSII/2017/23C), Department of Bioscience and Bioengineering and CIF-IITG for computing and instrument facilities. T.S. thanks CSIR for the Fellowship.

## Conflict of Interest

The authors declare no conflict of interest.

## Data Availability Statement

The data that support the findings of this study are available in the supplementary material of this article.

## Keywords

aggregation induced delayed emission, long-term bioimaging, mechanoluminescence, thermally activated delayed fluorescence, through-space charge-transfer

Received: November 8, 2024

Revised: January 6, 2025

Published online: January 28, 2025

- [1] a) Z. Li, D. Yang, C. Han, B. Zhao, H. Wang, Y. Man, P. Ma, P. Chang, D. Ma, H. Xu, *Angew. Chem., Int. Ed.* **2021**, *60*, 14846; b) X. Xiong, F. Song, J. Wang, Y. Zhang, Y. Xue, L. Sun, N. Jiang, P. Gao, L. Tian, X. Peng, *J. Am. Chem. Soc.* **2014**, *136*, 9590; c) H. Shi, L. Zou, K. Huang, H. Wang, C. Sun, S. Wang, H. Ma, Y. He, J. Wang, H. Yu, W. Yao, Z. An, Q. Zhao, W. Huang, *ACS Appl. Mater. Interfaces* **2019**, *11*, 18103; d) H. Zhang, H. Ma, W. Huang, W. Gong, Z. He, G. Huang, B. S. Li, B. Z. Tang, *Mater. Horiz.* **2021**, *8*, 2816.
- [2] J.-F. Cheng, Z.-H. Pan, K. Zhang, Y. Zhao, C.-K. Wang, L. Ding, M.-K. Fung, J. Fan, *Chem. Eng. J.* **2022**, *430*, 132744.
- [3] P. R. Bommireddy, C. S. Musalikunta, Y.-W. Lee, Y. Suh, M. Godumala, S.-H. Park, *J. Mater. Chem. C* **2024**, *12*, 6743.
- [4] B. Li, Z. Yang, W. Gong, X. Chen, D. W. Bruce, S. Wang, H. Ma, Y. Liu, W. Zhu, Z. Chi, Y. Wang, *Adv. Opt. Mater.* **2021**, *9*, 2100180.
- [5] Q. Li, Y. Wu, J. Cao, Y. Liu, Z. Wang, H. Zhu, H. Zhang, F. Huang, *Angew. Chem., Int. Ed.* **2022**, *61*, 202202381.
- [6] Q. Xue, G. Xie, *Adv. Opt. Mater.* **2021**, *9*, 2002204.
- [7] a) H. Tsujimoto, D.-G. Ha, G. Markopoulos, H. S. Chae, M. A. Baldo, T. M. Swager, *J. Am. Chem. Soc.* **2017**, *139*, 4894; b) Y. Song, M. Tian, R. Yu, L. He, *ACS Appl. Mater. Interfaces* **2021**, *13*, 60269; c) Y. Geng, A. D'Aleo, K. Inada, L.-S. Cui, J. U. Kim, H. Nakanotani, C. Adachi, *Angew. Chem., Int. Ed.* **2017**, *56*, 16536.
- [8] D. Barman, M. Annadhasan, R. Chandrasekar, P. K. Iyer, *Chem. Sci.* **2022**, *13*, 9004.
- [9] a) P. Rajamalli, P. Gandeepan, M.-J. Huang, C.-H. Cheng, *J. Mater. Chem. C* **2015**, *3*, 3329; b) L. Zhan, Z. Chen, S. Gong, Y. Xiang, F. Ni, X. Zeng, G. Xie, C. Yang, *Angew. Chem., Int. Ed.* **2019**, *131*, 17815.
- [10] a) K.-W. Lee, Y. Wan, Z. Huang, Q. Zhao, S. Li, C.-S. Lee, *Adv. Mater.* **2024**, *36*, 2306492; b) S. Gan, J. Zhou, T. A. Smith, H. Su, W. Luo, Y. Hong, Z. Zhao, B. Z. Tang, *Mater. Chem. Front.* **2017**, *1*, 2554.
- [11] S. Qi, S. Kim, V.-N. Nguyen, Y. Kim, G. Niu, G. Kim, S.-J. Kim, S. Park, J. Yoon, *ACS Appl. Mater. Interfaces* **2020**, *12*, 51293.
- [12] M. Y. Berezin, S. Achilefu, *Chem. Rev.* **2010**, *110*, 2641.
- [13] H. Gao, Z. Gao, D. Jiao, J. Zhang, X. Li, Q. Tang, Y. Shi, D. Ding, *Small* **2021**, *17*, 2005449.
- [14] a) M. Salimimarand, D. D. La, S. V. Bhosale, L. A. Jones, S. V. Bhosale, *Appl. Sci.* **2017**, *7*, 1119; b) D. D. L. a. Anuradha, M. Al Kobaisi, S. V. Bhosale, *Sci. Rep.* **2015**, *5*, 15652.
- [15] X. Wang, H. Ma, M. Gu, C. Lin, N. Gan, Z. Xie, H. Wang, L. Bian, L. Fu, S. Cai, Z. Chi, W. Yao, Z. An, H. Shi, W. Huang, *Chem. Mater.* **2019**, *31*, 5584.
- [16] D. Barman, P. K. Iyer, *J. Phys. Chem. C* **2023**, *127*, 2694.
- [17] A. Ekbote, S. M. Mobin, R. Misra, *J. Mater. Chem. C* **2020**, *8*, 3589.
- [18] D. Tahaoğlu, H. Usta, F. Alkan, *J. Phys. Chem. A* **2022**, *126*, 4199.
- [19] L. Tong, J. Yang, Y. Yang, Z. Liu, M. Fang, Z. Li, *ACS Mater. Lett.* **2024**, *6*, 2748.
- [20] J. Zhang, P. Alam, S. Zhang, H. Shen, L. Hu, H. H. Y. Sung, I. D. Williams, J. Sun, J. W. Y. Lam, H. Zhang, B. Z. Tang, *Nat. Commun.* **2022**, *13*, 3492.
- [21] T. Liu, X. Chen, J. Zhao, W. Wei, Z. Mao, W. Wu, S. Jiao, Y. Liu, Z. Yang, Z. Chi, *Chem. Sci.* **2021**, *12*, 5171.
- [22] C. Jiang, J. Miao, D. Zhang, Z. Wen, C. Yang, K. Li, *Research* **2022**, *2022*, 9892802.
- [23] M. A. El-Sayed, *J. Chem. Phys.* **1963**, *38*, 2834.
- [24] Y. Sun, Z. Lei, H. Ma, *J. Mater. Chem. C* **2022**, *10*, 14834.
- [25] B. Xu, J. He, Y. Mu, Q. Zhu, S. Wu, Y. Wang, Y. Zhang, C. Jin, C. Lo, Z. Chi, A. Lien, S. Liu, J. Xu, *Chem. Sci.* **2015**, *6*, 3236.
- [26] W. Luo, Y. Tang, X. Zhang, Z. Wu, G. Wang, *Adv. Opt. Mater.* **2023**, *11*, 202202259.
- [27] a) R. J. C. Brown, R. F. C. Brown, *J. Chem. Educ.* **2000**, *77*, 724; b) R. Pinal, *Org. Biomol. Chem.* **2004**, *2*, 2692.